

## RESEARCH ARTICLE

10.1029/2018JD028973

## Key Points:

- The aerosol concentration in the free troposphere was highest in late spring and summer and lowest in late summer and fall
- The aerosol particle depolarization ratio in the free troposphere was largest in winter and spring and smallest in summer
- The values of the particle depolarization ratio are consistent with a previously found mixture of liquid phase sulfate and soot particles

## Correspondence to:

T. Shibata,  
shibata\_takashi@nagoya-u.jp

## Citation:

Shibata, T., Shiraishi, K., Shiobara, M., Iwasaki, S., & Takano, T. (2018). Seasonal variations in high Arctic free tropospheric aerosols over Ny-Ålesund, Svalbard, observed by ground-based lidar. *Journal of Geophysical Research: Atmospheres*, 123, 12,353–12,367. <https://doi.org/10.1029/2018JD028973>

Received 13 MAY 2018

Accepted 24 OCT 2018

Accepted article online 26 OCT 2018

Published online 12 NOV 2018

## Author Contributions:

**Formal analysis:** T. Shibata**Funding acquisition:** T. Shibata**Investigation:** T. Shibata, K. Shiraishi, S. Iwasaki**Methodology:** T. Shibata, K. Shiraishi, M. Shiobara, T. Takano**Writing - original draft:** T. Shibata**Writing - review & editing:** T. Shibata

## Seasonal Variations in High Arctic Free Tropospheric Aerosols Over Ny-Ålesund, Svalbard, Observed by Ground-Based Lidar

T. Shibata<sup>1</sup> , K. Shiraishi<sup>2</sup>, M. Shiobara<sup>3</sup>, S. Iwasaki<sup>4</sup> , and T. Takano<sup>5</sup>

<sup>1</sup>Graduate School of Environmental Studies, Nagoya University, Nagoya, Japan, <sup>2</sup>Department of Earth System Science, Fukuoka University, Fukuoka, Japan, <sup>3</sup>National Institute of Polar Research, Tokyo, Japan, <sup>4</sup>National Defense Academy of Japan, Kanagawa, Japan, <sup>5</sup>Graduate School of Engineering, Chiba University, Chiba, Japan

**Abstract** Free tropospheric aerosols over the high Arctic were observed by lidar for about 4 years from March 2014 at Ny-Ålesund (78.9°N, 11.9°E). Vertical profiles of aerosol backscattering coefficients at two wavelengths, 532 and 1,064 nm, and depolarization ratio at one wavelength, 532 nm, are derived from these observations. The aerosol backscattering coefficient, the particle depolarization ratio, and the color ratio (the ratio of the backscattering coefficients at the two wavelengths) are roughly proportional to mass concentration, nonsphericity, and size of the aerosol particles, respectively. The aerosol backscattering coefficients indicate that monthly averaged concentration of aerosols was largest in the lowest free troposphere at about 1 km in altitude and was an order of magnitude less at an about 10 km in altitude and that the concentration of aerosols was highest from late spring to summer and lowest from late summer to fall. The depolarization ratio was less than a few percent in the troposphere during the four observed years. The depolarization ratio and the color ratio were greatest from winter to spring and smallest from summer to fall. The maxima in the monthly averaged nonsphericity and size precede the maxima in the monthly averaged concentration by a few months, indicating a seasonal change in the morphology or the characteristics of the aerosol particles. The small particle depolarization ratio of less than a few percent is consistent with previous findings that Arctic free tropospheric aerosol particles in spring are composed of a mixture of liquid phase sulfate and soot particles.

### 1. Introduction

Arctic warming is countered to some degree by aerosols (Breider et al., 2014, 2017; Najafi et al., 2015). Because more accurate aerosol reproduction in climate models is crucial for reliable simulations of the warming, observations of Arctic aerosols provide key information for Arctic climate studies. Many observational studies on Arctic aerosols have been performed, including those on the well-known “Arctic haze” (e.g., Quinn et al., 2007; Shaw, 1975, 1995). However, because most of these observational aerosol studies have been conducted on the ground, the vertical and temporal aerosol structures remain unclear, especially in the free troposphere over the Arctic.

Various intensive research efforts are being made to understand the impacts of aerosols on atmospheric processes. Of these efforts, observations of the spatial distribution and the temporal variation provide the most basic information concerning aerosols for further studies on their impacts. Monitoring of aerosols is conducted at multiple observational sites at middle and low latitudes (e.g., Dubovik et al., 2000). Lidar systems provide vertical profiles of aerosols and their temporal variations at several stations primarily in the midlatitudes (e.g., Pappalardo et al., 2014; Shimizu et al., 2016). Even though substantial amounts of observations are executed at these latitudes, long-term lidar observations for periods of several years in the high Arctic (>70°N) are very limited and nearly all lidar observations there have been made as campaign bases (e.g., Nott & Duck, 2011).

Space-borne instruments, such as the Cloud-Aerosol Lidar with Orthogonal Polarization (CALIOP) onboard the Cloud-Aerosol Lidar and Infrared Pathfinder Satellite Observation (CALIPSO) satellite or the Stratospheric Gas Experiment (SAGE), provide observations of the global distribution of aerosols, including in the Arctic region, and their temporal variations. Observations of the Arctic region from space, however, are significantly affected by its unique condition of having very different background solar radiation levels

between the polar night in winter and the midnight Sun in summer, that is, in the seasons without sunrise or sunset. The detection sensitivity of CALIOP in the troposphere is several tens of percent higher at night than during the day (Winker et al., 2009). Observations by SAGE in the high Arctic region are not possible in seasons without a sunrise or a sunset.

Monitoring of Arctic aerosols from the ground is performed at several coastal sites surrounding the Arctic Ocean. Arctic aerosols have maximum concentrations in the spring at ground level and are referred to as Arctic haze (e.g., Quinn et al., 2007).

Herber et al. (2002) presented the aerosol optical depth (AOD) over Ny-Ålesund since 1991 using a photometer. They recorded data regardless of the season using not only the Sun but also the Moon and stars during periods when the Sun did not rise. Their results indicated that the AOD has maximum values in April and May. The higher concentration of aerosol particles at the lowest altitudes in the boundary layer is likely the primary contributor to the AOD observed at the ground.

Treffeisen et al. (2006) used approximately 20 years of SAGE II and III data to calculate the seasonal variation in the aerosol characteristics in the upper troposphere. Their results indicate that the extinction of aerosols at altitudes higher than 6 km is maximized in May and June.

Di Pierro et al. (2013) used Level 2 CALIOP data to examine the spatial distribution and seasonal variation in the Arctic tropospheric aerosols. Their data analysis, which took into account the difference in the sensitivity between the day and night observations, demonstrated that the extinction of aerosols is maximum in December and January at altitudes lower than 2 km and in April and May at free tropospheric altitudes over the Arctic.

Therefore, there is a difference of a few months in the seasonal variation in the extinction in the free troposphere between measurements by SAGE and CALIOP from space. At the altitude of the boundary layer, the difference between the seasons is considerable for the maximum extinction values measured in spring (March, April, and May) by ground-based observations and in winter (December and January) by CALIOP. As a result, there are nonnegligible differences in the observed seasonal variations in the extinction, or density, of aerosols over the high Arctic in results obtained using different observational methods.

There have been attempts to apply lidar to observe tropospheric aerosols in the high Arctic (e.g., Ishii et al., 1999; Ishii et al., 2001; Leaitch et al., 1986; Ritter et al., 2016). However, most attempts have been limited to certain periods of time during the year. Therefore, seasonal variations in the aerosols have not been described well by these observations.

We installed an Nd:YAG laser-based Mie depolarization lidar system in Ny-Ålesund in March 2014 and performed nonstop observations for approximately 4 years. The backscattering coefficient of the aerosols at 532 and 1064 nm and the particle depolarization ratio at 532 nm were obtained using the lidar system. The lidar system observed all atmospheric particles or molecules, aerosols, clouds, and precipitation. In this study, however, only the results for conditions without clouds or precipitation, that is, only the aerosol results, are presented. Because the data under this condition can be calibrated using conventional normalization methods (e.g., Russell et al., 1979) at the lowest stratospheric altitudes, the results can be used to obtain the seasonal variations in the aerosols in the troposphere.

In sections 2 and 3, the technical aspects of the lidar observations and data analysis method are described, respectively. In section 4, the results of the observations and the seasonal variations in the observed parameters are presented. In sections 5 and 6, the discussion and the summary and conclusions are presented, respectively. In Appendices A, B, and C, the cloud removal procedure and the depolarization ratio analysis are described.

## 2. Lidar System and Observations

A lidar system was installed to observe Arctic tropospheric aerosols and clouds at the Arctic station of the Japanese National Institute of Polar Research in Ny-Ålesund, Svalbard, in March 2014. Ny-Ålesund is a town that is maintained for scientific research purposes in the Arctic. The same station has been used for observations of polar stratospheric clouds primarily in the 1990s (Shibata et al., 1999).

The lidar system detects backscattering signals at the fundamental wavelength, 1,064 nm, and two polarization signal components at the second harmonic generation wavelength of the laser, 532 nm. The

**Table 1**  
*Characteristics of the Lidar System*

Transmitter	
Laser:	Nd:YAG laser with second harmonic generation (ULTRA, BigSky)
Output:	0.3 W (30 mJ/pulse, 10 pulses/s), 0.1 W at 1,064 nm, 0.2 W at 532 nm
Beam divergence:	0.1 mrad
Receiver	
Telescope:	ϕ20 cm, f/10, (Meade LX200)
Field of view:	0.5 mrad
Interference filter:	0.3 nm FWHM (Barr)
Detector:	PMT for 532 nm (HAMAMATSU H956-08) APD for 1064 nm (Licel APD-3.0)
Transient recorder:	12-bit, 20 MHz (Licel TR20-160)
Range resolution:	15 m
Temporal resolution:	1 min
Observed parameters:	Backscattering coefficients at 532 and 1,064 nm Depolarization ratio at 532 nm

characteristics of the lidar system are summarized in Table 1. The signal at 532 nm is separated into parallel and perpendicular components of the polarization with respect to the polarization plane of the linearly polarized laser pulse using a cubic polarization prism. The signal of the parallel component is further separated into a weaker signal (1%) for altitudes lower than 7.5 km and a stronger signal (99%) for altitudes higher than 7.5 km using an antireflection coated glass window to increase the dynamic range of the parallel component of the signal. All the signals at 532 nm, the two with parallel polarization and the one with perpendicular polarization, are detected using photomultiplier tubes (PMT; HAMAMATSU, H956-08). The signal at 1,064 nm is detected via an Si-avalanche photodiode module (APD; Licel, APD-3.0). The electrical signals from these detectors are sampled via 12-bit transient recorders (Licel, TR20-160). The signals from the PMT are also simultaneously sampled in photon-counting mode using the multichannel scaler function of these transient recorders.

The lidar system is installed in a 20-foot shipping container modified for the lidar system. The lidar is pointed 4° off the zenith. This angle is set to detect horizontally oriented ice cloud particles (Platt et al., 1978). The observations are made through a 30° slanted antireflection coated glass

window located at the top of the container. Inside condensation by dew and outside cover by snow or ice on the window are prevented by maintaining a flow of air to the window in the heated room inside the container. The repetition rate of the laser pulse is 10 pulses per second. The data for 600 laser pulses, or 1 min, are accumulated via transient recorders with 15-m vertical resolution and stored in a PC. The lidar system can be remotely controlled via the Internet.

### 3. Lidar Data

The signal components of the lidar,  $P_{\lambda, \parallel \text{ or } \perp}(r)$ , a distance  $r$  from the lidar system are expressed as

$$P_{\lambda, \parallel \text{ or } \perp}(r) = K_{\lambda, \parallel \text{ or } \perp} \frac{\beta_{M\lambda, \parallel \text{ or } \perp}(r) + \beta_{R\lambda, \parallel \text{ or } \perp}(r)}{r^2} \exp(-2 \int_0^r (\sigma_{\lambda M}(r) + \sigma_{\lambda R}(r) + \sigma_{\lambda O_3}(r)) dr), \quad (1)$$

where the subscripts  $\lambda$ ,  $\perp$ , and  $\parallel$  indicate the wavelength and the perpendicular and parallel polarization components of the signal, respectively. The polarization components are only available at the wavelength of 532 nm, as described in the previous section.  $K$  is the constant for each component,  $\beta$  is the backscattering coefficient,  $\sigma$  is the extinction or absorption coefficient, and the subscripts  $M$ ,  $R$ , and  $O_3$  indicate Mie scattering, Rayleigh scattering, and absorption by ozone, respectively. These subscripts are also used in subsequent equations. We derived vertical profiles from equation (1) using the relation  $r \cos \theta = z - z_0$ , where  $\theta$  is the pointing angle of the lidar from the zenith (4° in our system),  $z$  is the altitude above sea level at a distance  $r$ , and  $z_0$  is the altitude of the lidar system above sea level.

The lidar data that are longer than 10 min in 1 day under conditions without clouds are averaged. The cloud removal procedure is summarized in Appendix A. The length of time covered by the average data varies from 10 min to several hours depending on the length of the interval without clouds or precipitation. We obtained one averaged cloud-free profile per day. There were 511 days (or profiles) with such cloud-free periods during the four years of lidar observations. These days with cloud-free time intervals were nearly uniformly distributed in each month of the four years. Table 2 shows the number of days (profiles) per month for the four years. The cloud-free profiles may introduce a bias in the results if the vertical profiles of the aerosols have cloud dependence. However, Di Pierro et al. (2013) indicated that the difference in the extinction of aerosols under cloudy conditions observed by CALIPSO is less than 10%; therefore, the bias was assumed to be negligible.

Figure 1a shows an example of a 1-day plot of the Rayleigh-backscattering-coefficient-subtracted normalized range-corrected signal, or the Rayleigh-backscattering-coefficient-subtracted attenuated-backscattering coefficient without correction for attenuation, at the wavelength of 1,064 nm on May 20, 2014. To calculate the normalized attenuated-backscattering coefficient in Figure 1a, the normalization constant obtained for

**Table 2**  
Number of Days (Profiles) in Each Month of the Four Years and the Total Number of Profiles per Month Used for the Analysis in This Paper

Month/year	2014	2015	2016	2017	Total
January		9	12	14	35
February		11	15	12	38
March	8	4	15	14	41
April	21	11	16	19	67
May	14	10	9	18	51
June	9	10	7	11	37
July	5	16	12	14	47
August	9	12	13	11	45
September	6	7	8	8	29
October	11	9	7	8	35
November	12	8	11	13	44
December	13	13	13	3	42

the profiles taken in the clear time period (Figure 1b) was used for all the 1-min profiles on this day. The Rayleigh-backscattering coefficient is calculated from the sounding data taken over Ny-Ålesund on the same day. Because the overlap between the laser beam and the field of view of the receiver is insufficient from the ground to an altitude of 600 m (2 km from June to September in 2014), the plotted values are smaller than the actual value in this lowest altitude range. There is a signal from clouds from 0 UT to 11 UT at altitudes from 1 to 3 km and from 14 UT to 24 UT at altitudes from 1 to 6 km. The signal is nearly completely attenuated above the clouds on this day. There is also a signal from thin clouds within the clear time interval from 11 UT to 14 UT for short periods near 12:40 UT and 14:40 UT at altitudes of 1 and 2 km, respectively.

We frequently observed oscillations of the signal in the height direction at 1,064 nm above the clouds, as shown in Figure 1a. This is caused by the APD detector module used by the system and is an artificial oscillation following the strong signal from the clouds. The oscillation is sometimes

observed under the no-cloud condition as well. Because the oscillation has a regular waveform with a fixed wavelength and phase, we digitally removed this oscillation from the signal.

### 3.1. Backscattering Coefficient of the Aerosols

Figure 1b shows the range- and attenuation-corrected (see below) profile of the signal at 1,064 nm (red) and the total component (parallel plus perpendicular) signal at 532 nm (green) averaged in the clear time interval from 13:48 UT to 14:00 UT on May 20, 2014. In Figure 1b, the Rayleigh-backscattering coefficients at 532 nm (solid black) and 1,064 nm (dotted black) calculated from the sounding data at 12 UT on this day over Ny-Ålesund by the Alfred Wegener Institute are also included. The profiles are normalized to the lower stratosphere (see below). The profile of the range-corrected and sensitivity-adjusted (see section 3.2) perpendicular polarization signal component (blue) is also shown in Figure 1b. We used the range between 12 and 15 km for the normalization of the signal at 532 nm with the Rayleigh-backscattering coefficient calculated from the sounding data. The backscatter ratio,  $R_{\lambda}$ , at an altitude  $z$  and a wavelength  $\lambda$  is defined as

$$R_{\lambda}(z) = \frac{\beta_{M_{\lambda}}(z) + \beta_{R_{\lambda}}(z)}{\beta_{R_{\lambda}}(z)}, \quad (2)$$

where  $\beta$  ( $=\beta_{\parallel} + \beta_{\perp}$ ) is the total backscattering coefficient of the two polarization components. To normalize the data at 532 nm, the average  $R_{532}$  at altitudes between 12 and 15 km,  $R_0$ , was assumed to be 1.10, which is the average value from a stratospheric aerosol analysis using the same lidar system. This value is consistent with typical lower stratospheric values without volcanic disturbances over Tsukuba, Japan (Sakai et al., 2016).

Even though a fixed value of 1.10 was used as the value of  $R_0$  in this study, the stratospheric aerosol analysis found that the values of  $R_0$  presented a slight seasonal variation; values were a few percent lower in summer and higher in winter than the fixed value of 1.10. The few percent negative or positive variations in  $R_0$  caused several percent negative or positive variations in  $\beta_{M_{532}}$ , respectively. The appearance of polar stratospheric clouds at altitudes between 12 and 15 km during January and February in 2016 led to averaged values of  $R_0$  of approximately 1.2 in these months. Assuming a fixed  $R_0$  (1.10), therefore, introduced a 20% underestimation in  $\beta_{M_{532}}$  during these two months. However, these variations in  $R_0$  from the fixed value do not affect the conclusions of this study.

The backscattering coefficient was calculated using the Fernald method to correct for attenuation (Fernald, 1984) by assuming an extinction-to-backscatter ratio (a lidar ratio),  $\sigma_{M_{\lambda}}/\beta_{M_{\lambda}}$ , of 40 sr at both 532 and 1,064 nm. These ratios are approximate averages of the values used in the CALIOP data retrieval (Catrall et al., 2005; Omar et al., 2005) and take into account the results of ground-based Raman lidar observations over Ny-Ålesund (Ritter et al., 2016). The several tens of percent decrease in the assumed lidar ratio resulted in

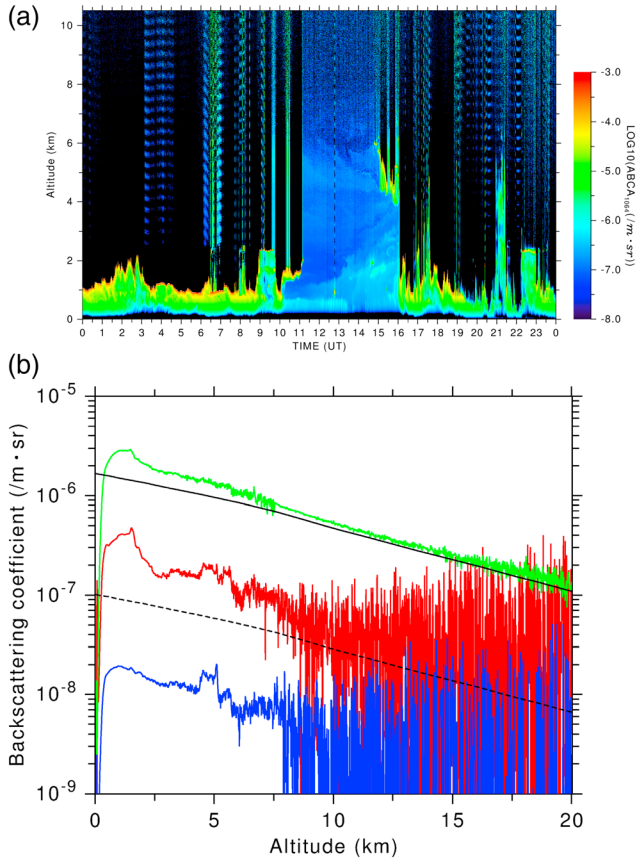


**Figure 1.** (a) Plot of the Rayleigh-backscattering coefficient-subtracted attenuated-backscattering coefficient for 1 day observed on 20 May 2014. (b) The range- and attenuation-corrected profiles of the signal at 1,064 nm (red), the total component signal at 532 nm (green), and the sensitivity-adjusted perpendicular polarization signal component (blue) observed between 13:48 UT and 14:00 UT on 20 May 2014. The Rayleigh-backscattering coefficient at 532 nm (black) and 1,064 nm (dotted black) calculated from the sounding data observed over Ny-Ålesund near 12 UT on the same day.

an increase in  $\beta_{M532}$  in the lower and upper free troposphere by several percent and less than 1%, respectively. The uncertainty in the lidar ratio does not affect the conclusions of this study.

The color ratio,  $\gamma$ , is defined by the ratio of the particle backscattering coefficient at 1,064 nm to that at 532 nm:

$$\gamma(z) = \frac{\beta_{M\ 1064}(z)}{\beta_{M\ 532}(z)}. \quad (3)$$

The color ratio  $\gamma$  is roughly proportional to the size of the particles (Shibata & Yang, 2010). We assumed that the color ratio of the aerosols at altitudes between 10.5 and 12 km is 0.5 (Shibata et al., 2012). With this assumption, we can calculate the averaged R1064 from  $R_{532}$  in this altitude range; that is, we can normalize the data at 1,064 nm.

### 3.2. Depolarization Ratio

In this paper, the volume depolarization ratio,  $\delta_V$ , at an altitude  $z$  is defined as

$$\delta_V(z) = \frac{\beta_{M\perp}(z) + \beta_{R\perp}(z)}{\beta_{M\parallel}(z) + \beta_{R\parallel}(z) + \beta_{M\perp}(z) + \beta_{R\perp}(z)}. \quad (4)$$

Because the depolarization ratio is obtained only at the wavelength 532 nm, the subscript indicating the wavelength (532) is omitted in this subsection. The volume depolarization ratio,  $\delta_V(z)$ , includes depolarization due to both atmospheric molecules and aerosol particles.

The particle depolarization ratio,  $\delta_P$ , including only depolarization by aerosol particles, is a parameter describing the sphericity of the particles and is defined as

$$\delta_P(z) = \frac{\beta_{M\perp}(z)}{\beta_{M\parallel}(z) + \beta_{M\perp}(z)}. \quad (5)$$

In Mie scattering theory,  $\delta_P$  is exactly zero if the particles are perfect spheres or composed of liquid in the atmosphere. A larger value of  $\delta_P$  indicates a higher nonsphericity of the particles (e.g., Shibata & Yang, 2010).

The volume depolarization ratio can be estimated from the observed signal components of equation (1) as

$$\delta'_V(z) = \frac{gP_{\perp}(z)}{P_{\parallel}(z) + gP_{\perp}(z)}, \quad (6)$$

where  $g$  is a factor used to adjust for the differences in the sensitivities of detecting the perpendicular and parallel polarization signal components. The factor  $g$  is estimated experimentally, as described in Appendix B. For an ideal polarization lidar system without cross talk between the two components and without a vertical polarization component of the laser pulse, if we know the accurate  $g$  value without error, the estimated  $\delta'_V$  in equation (6) from the observations is exactly equal to the definition of  $\delta_V$  in equation (4). However,  $\delta'_V$  in an actual system needs to be corrected for the nonideal components of the lidar system. In Appendix C, the method to estimate  $\delta_V$  from  $\delta'_V$  and  $R(z)$  is described. Using this estimated  $\delta_V$ ,  $\delta_P$  is obtained as

$$\delta_P(z) = \frac{\delta_V(z) - \delta_{am}R(z)^{-1}}{1 - R(z)^{-1}}, \quad (7)$$

where  $\delta_{am}$  is the depolarization ratio of the atmospheric molecules (Adachi et al., 2001).

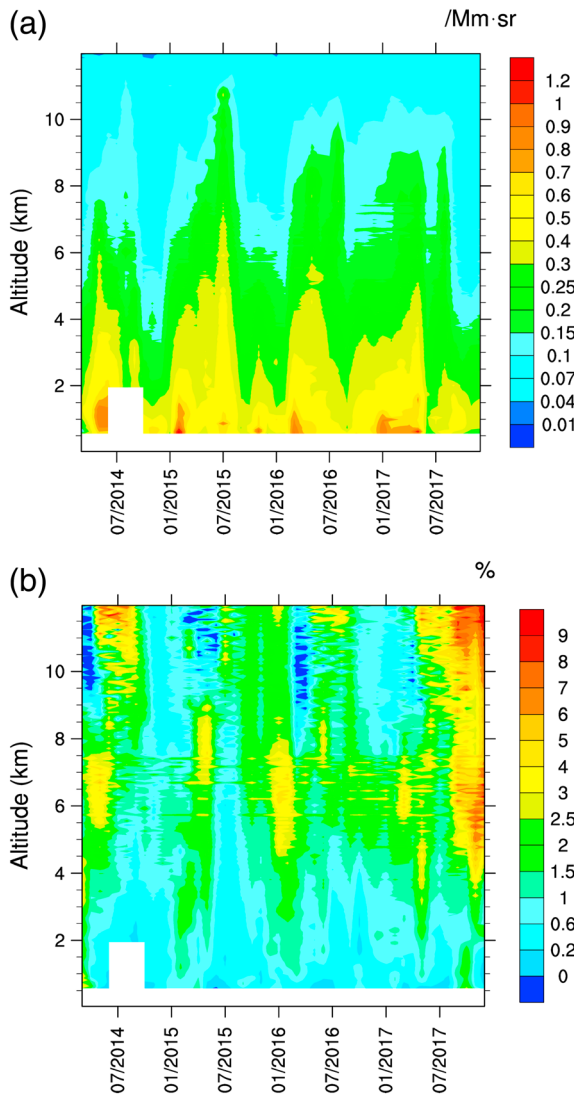


**Figure 2.** (a) Averaged backscattering coefficient at 532 nm ( $\beta_{M532}$ ) for each month of the four years,  $\overline{\beta_{M532}}$ , and (b) averaged particle depolarization ratio at 532 nm (%) for each month of the four years,  $\overline{\delta_p}$ , from March 2014 to December 2017.

#### 4. Results

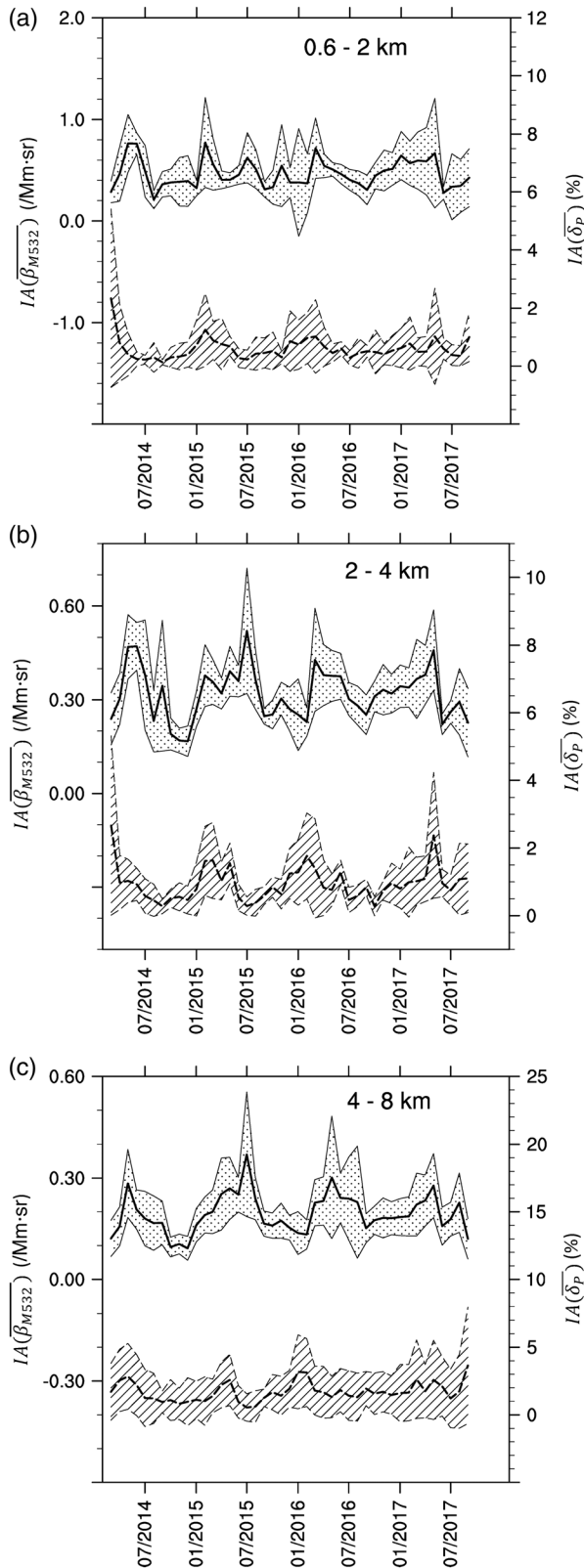
Figure 2a shows the averaged  $\overline{\beta_{M532}}$  for each month of the four observed years,  $\overline{\beta_{M532}}$ , from March 2014 to December 2017. We can see that  $\overline{\beta_{M532}}$  decreased with altitude;  $\overline{\beta_{M532}}$  was near 0.5–1/Mm·sr at an altitude lower than approximately 1 km and 0.1–0.2/Mm·sr at an altitude of approximately 10 km. The decrease in  $\overline{\beta_{M532}}$  with altitude was approximately an order of magnitude through the troposphere. At an altitude higher than 2 km, we can see a clear cyclic seasonal variation in  $\overline{\beta_{M532}}$  showing increases in the first half of the year, with the largest values from May to July, and decreases in August or September, with the smallest values occurring in the following months. At altitudes lower than 2 km, even though the seasonal variation was not as clear as at higher altitudes,  $\overline{\beta_{M532}}$  had larger values in the spring and other larger values were found in fall and winter.

Figure 2b shows the averaged  $\overline{\delta_p}$  for each month of the four years,  $\overline{\delta_p}$ .  $\overline{\delta_p}$  was smaller than a few percent prior to July 2017. The largest values of  $\overline{\delta_p}$ , a few percent, occurred during winter and spring at altitudes from 5 to 8 km; the smallest value, at nearly 0%, occurred in the summer at altitudes lower than 4 km.  $\overline{\delta_p}$  has smaller values at altitudes lower than 4 km, where  $\overline{\delta_p}$  was smaller than 1% in the summer and fall.  $\overline{\delta_p}$  was larger at higher altitudes but was smaller than 1% at an altitude near 5 km in the summer. Larger values of  $\overline{\delta_p}$  of approximately 5% were observed from January to March at altitudes from 5 to 8 km. Smaller values of less than 2% percent were observed in summer and fall in the same altitude range. The large values of  $\overline{\delta_p}$  (red color) after September 2017 at altitudes higher than 5 km were caused by aerosols from intense wildfire events in British Columbia, Canada, in August 2017 (EGU General Assembly, 8–13 April 2018, Vienna, Austria, session: “Unprecedented Wildfires and Smoke Plumes—2017 and Beyond”).

We can see in Figures 2a and 2b that  $\overline{\delta_p}$  near an altitude of 4 km had its largest values when  $\overline{\beta_{M532}}$  was increasing. In Figure 3, the temporal variations in the altitude-interval-averaged  $\overline{\beta_{M532}}$  and  $\overline{\delta_p}$ ,  $IA(\overline{\beta_{M532}})$  and  $IA(\overline{\delta_p})$ , respectively, in three altitude intervals are depicted. Figure 3a shows the averaged altitude interval of 0.6–2 km, Figure 3b shows the interval of 2–4 km, and Figure 3c shows the interval of 4–8 km.

The bold solid and broken lines indicate  $IA(\overline{\beta_{M532}})$  and  $IA(\overline{\delta_p})$ , respectively, and the thin solid and broken lines and the shading between them indicate the range of one standard deviation. We can see the difference in the timing of the temporal variations for  $IA(\overline{\beta_{M532}})$  and  $IA(\overline{\delta_p})$ . For the altitude intervals in Figures 3b and 3c, the change in  $IA(\overline{\delta_p})$  takes place a few months prior to the change in  $IA(\overline{\beta_{M532}})$  in 2014, 2015, and 2016. However, this offset is not as obvious in 2017. This is partly due to the influence of the intense wild fires in British Columbia, Canada, during that year.

Figure 4a shows the averaged  $\overline{\beta_{M1064}}$  for each month of the four years,  $\overline{\beta_{M1064}}$ . The values of  $\overline{\beta_{M1064}}$  are smaller than those of  $\overline{\beta_{M532}}$  (Figure 2a) following the wavelength dependence of aerosol backscattering. The characteristics of the relative vertical and temporal variations of  $\overline{\beta_{M1064}}$  are similar to the variations in  $\overline{\beta_{M532}}$ :  $\overline{\beta_{M1064}}$  also decreased with altitude and was 0.2–0.5/Mm·sr at altitudes lower than approximately 1 km and 0.01–0.07/Mm·sr at an altitude of 10 km. At altitudes higher than 2 km, there are clear cyclical seasonal variations in  $\overline{\beta_{M1064}}$ ; at altitudes lower than 2 km,  $\overline{\beta_{M1064}}$  had larger values in the spring, fall, and winter than in the summer.



**Figure 3.** The temporal variation in the altitude-interval-averaged  $\overline{\beta_{M532}}$  and  $\overline{\delta_p}$  in three averaged altitude intervals: (a) 0.6–2 km, (b) 2–4 km, and (c) 4–8 km. The bold (broken) line is the altitude-interval-averaged  $\overline{\beta_{M532}}$  ( $\overline{\delta_p}$ ), and the thin (broken) lines show the range of one standard deviation.

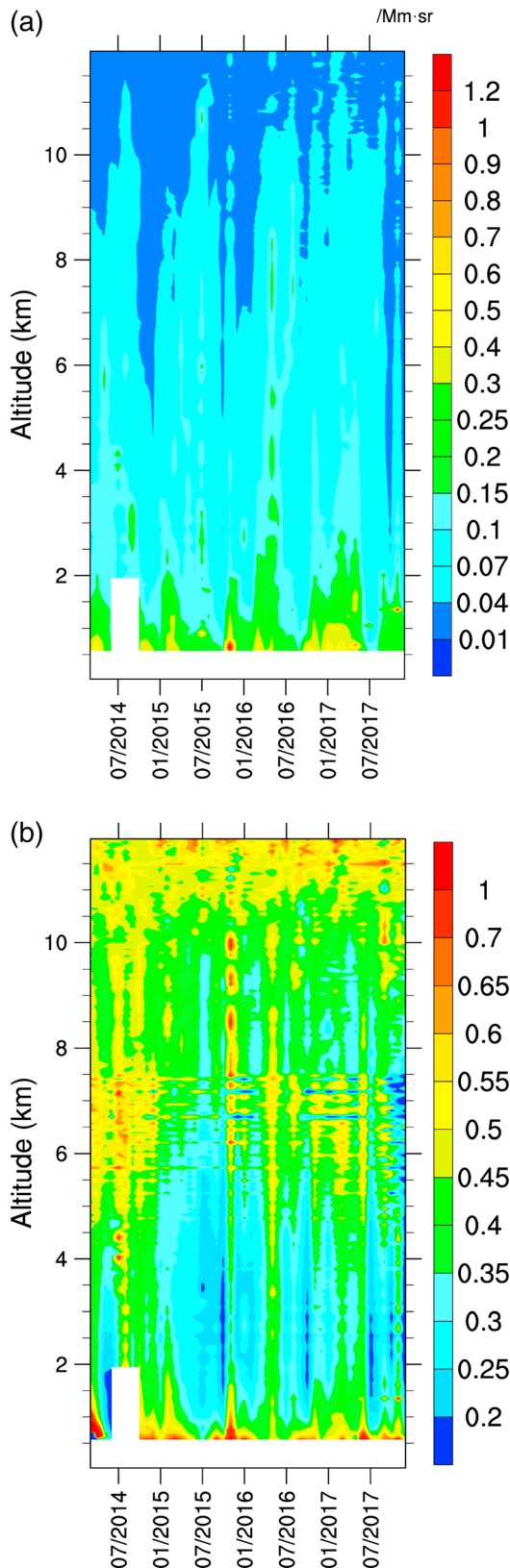
Figure 4b shows the averaged  $\gamma$  for each month of the four years,  $\overline{\gamma}$ , obtained from the backscattering coefficient at the two wavelengths. In the calculation of  $\overline{\gamma}$ ,  $\gamma$  for each profile was calculated first and then the values in a month were averaged from the calculated  $\gamma$  values. In Figure 4b,  $\overline{\gamma}$  had smaller values at altitudes from 1 to 5 km and larger values at altitudes lower than 1 km and higher than 5 km. Even though the seasonal cyclic variation is not as clear as in  $\overline{\beta_{M532}}$  or  $\overline{\delta_p}$ ,  $\overline{\gamma}$  has smaller values in the summer near altitudes from 2 to 4 km.

Figure 5 depicts the relative standard deviation (RSD) of (a)  $\beta_{M532}$ , (b)  $\delta_p$ , and (c)  $\gamma$ , whose monthly averages are shown in Figures 2 and 4b. Because the detector for the weaker signal intensity is used at altitudes lower than 7.5 km, the RSDs of all three parameters have vertical wavy structures at altitudes between 5 and 7.5 km and are larger than the RSDs at altitudes higher than 7.5 km in some seasons of years when the signal with the stronger intensity was used, as mentioned in section 2. The RSD of  $\beta_{M532}$  (Figure 5a) is approximately 20–40% at most altitudes but is as large as 50–80% at altitudes near 6–7 km. Even though this tendency is similar for  $\gamma$ , the RSD of  $\gamma$  (Figure 5c) is larger than 100% in some months near altitudes of 6–7 km. The RSD of  $\delta_p$  (Figure 5b) is much larger than the RSDs of  $\beta_{M532}$  and  $\gamma$ . This is partly due to the method used to derive  $\delta_p$  from  $\delta_v$  using  $R$ , as described in section 3.2. The values of  $\delta_p$  that are estimated at smaller  $R$  expand the error in  $\delta_v$ . The RSD of  $\delta_p$  in Figure 5b ranges from 40% to 100% at altitudes between 2 and 6 km; when  $\delta_p$  has its maximum values in Figure 2b, the RSD is as large as 500% at altitudes higher than 8 km and when  $\delta_p$  has its minimum values in Figure 2b.

### 5. Discussion

Figure 6a shows the averaged  $\overline{\beta_{M532}}$  for the same months throughout the four years of the observations,  $\overline{\beta_{M532}}$ . The temporal variation in the height of  $\overline{\beta_{M532}}$  with, for example, a value of 0.15/Mm-sr, the border between light blue and green, showed a highest altitude at approximately 8 and 10 km in May and August, respectively. The SAGE-observed extinctions at these altitudes in the same months are approximately 6 and 3/Mm, respectively, as shown in Figure 11 in Treffeisen et al. (2006). If we use our assumed extinction-to-backscatter ratio, 40 sr, to convert this  $\overline{\beta_{M532}}$ , 0.15/Mm-sr, the converted extinction is 6.0/Mm. Even though there are differences in the years of the observations, the difference is within a factor of two in August and the values show good agreement in May. If we focus on the variation in the altitude of the 3/Mm extinction, the SAGE observations show an earlier decrease in altitude in June or July than our ground-based lidar, which shows a decrease in September. The difference in the month of the decrease could be caused by the difference in the observed years (Figure 2a). In addition, the latitudes of the SAGE observations could also cause this difference. The SAGE observations are limited to latitudes where there are sunrises and sunsets; therefore, observations in midsummer and midwinter are only possible in the lower Arctic regions.

We can see in Figure 6a that the highest concentration of aerosols was from May to August in the free troposphere at altitudes higher than 5 km. These months were very different from the results of the CALIOP-



**Figure 4.** (a) Averaged backscattering coefficient at 1,064 nm ( $\beta_{M1064}$ ) and (b) averaged color ratio for each month of the four years,  $\bar{\gamma}$ , from March 2014 to December 2017.

observed aerosols. As mentioned in the introduction, Di Pierro et al. (2013) showed that the extinction of aerosols is maximum in April and May at free tropospheric altitudes over the high and low Arctic, respectively. We need to be careful because there are large differences between the sensitivities of CALIOP and our ground-based lidar. The detection limit of CALIOP in the upper troposphere is approximately 1.0/Mm·sr (Winker et al., 2009). Conversely, the detection limit of our ground-based lidar is approximately 0.01/Mm·sr. Therefore, CALIOP is observing high-concentration aerosol events, whereas the ground-based lidar is observing a more complete representation of the atmospheric aerosols. The difference in detection sensitivity between these two methods could result in a difference in the type of observed aerosols, such as biomass burning or dust aerosols with the events of high concentrations or background aerosols with lower concentrations. This is likely one of the reasons for the difference in the months with the highest concentration of aerosols.

The detection limit of the SAGE observations is less than approximately 0.5/Mm. Because the detection limit of the ground-based lidar multiplied by the lidar ratio is 0.4/Mm, the detection limit of SAGE and the detection limit of the ground-based lidar are nearly the same. Therefore, the better agreement between the observations by SAGE and the ground-based lidar may be due to their comparable detection limits.

Figure 7 shows the AOD calculated from the monthly averaged vertically integrated  $\overline{\beta_{M532}}$  at altitudes from 0.6 to 12 km multiplied by the lidar ratio. The upper and lower limits of the AOD were taken roughly from Figure 7 in Herber et al. (2002) as observed via a photometer. The AOD observed via lidar with a lidar ratio of 40 sr (solid line) was within the upper and lower limits from January to June but was larger than the upper limits from July to December. Assuming that  $\beta_{M532}$  in the unobserved altitude range lower than 0.6 km has the same value as that at 0.6 km, the AOD of this range was estimated to be from 0.01 to 0.02. Therefore, the AOD observed via lidar from the ground was larger than the plotted values by approximately these amounts. Even though the reason for this discrepancy is uncertain, larger AOD values obtained from  $\beta_{M532}$  may be caused by a suboptimal assumed lidar ratio. For example, assuming 25 sr as the lidar ratio led to an AOD within the range of the photometer observations (the thin solid line in Figure 7). However, it is not known whether the lidar AOD was larger than the photometer-observed upper limit or if a smaller lidar ratio and/or a smaller  $R_0$  should have been assumed.

The secondary maxima in July for  $\overline{\beta_{M532}}$  and in July 2015 for  $\overline{\beta_{M532}}$ , seen in Figures 6a and 2a, respectively, may have been caused by the reported smoke events in Ny-Ålesund from biomass burning during that month (Lisok et al., 2018). The data from 10 and 11 July, when the smoke concentration was the highest, were not included when calculating  $\overline{\beta_{M532}}$  or  $\overline{\beta_{M532}}$  due to the poor signal-to-noise ratio at an altitude of 12–15 km caused by the high extinction of the laser light through the smoke clouds. Therefore, the highest values of  $\beta_{M532}$  caused by smoke were not included in the average values. Small increases in the aerosols caused by biomass burning in the summer could have increased  $\overline{\beta_{M532}}$  or  $\overline{\beta_{M532}}$ ; however, identifying the source of this increase could be difficult.

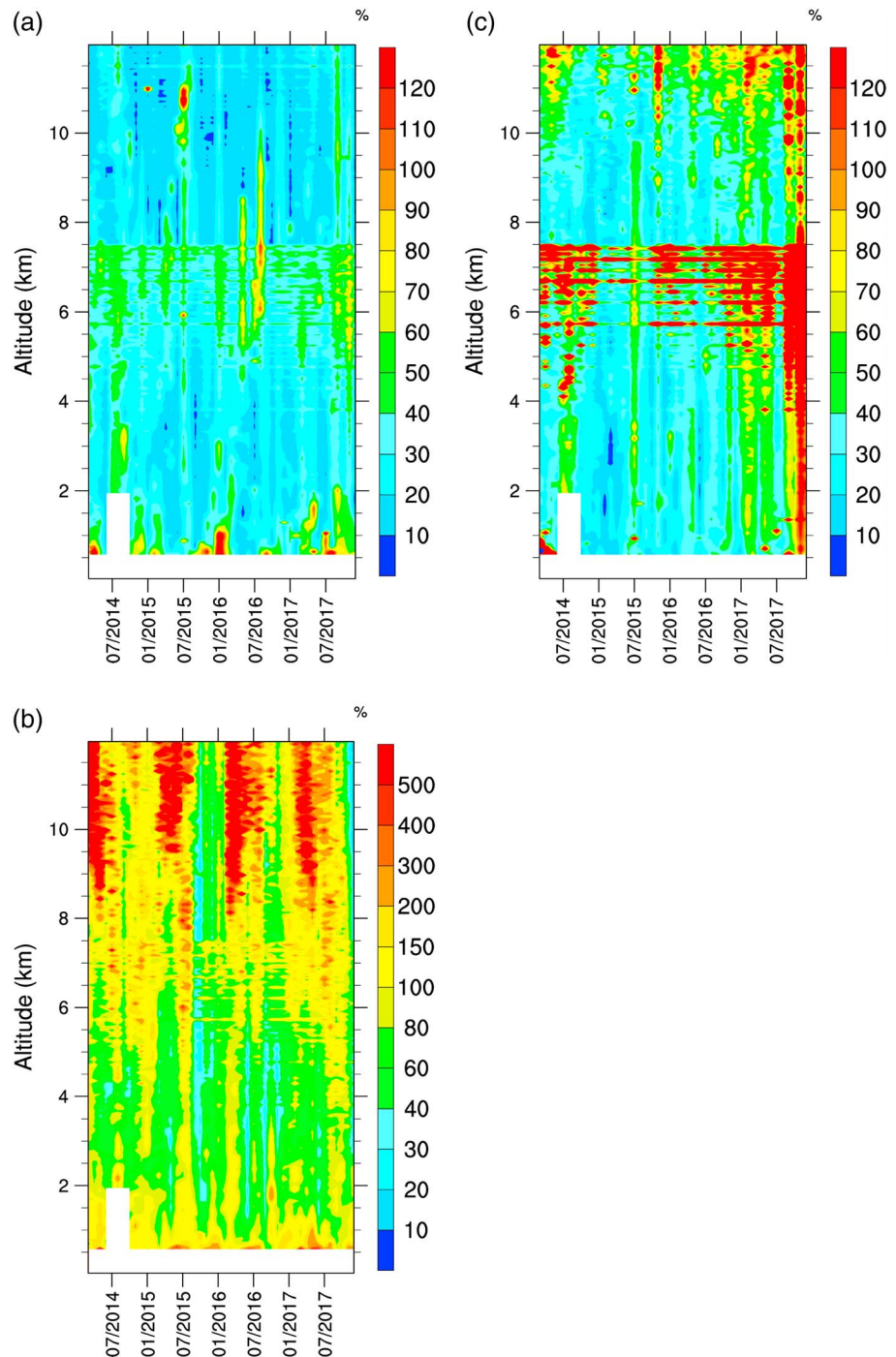


**Figure 5.** Relative standard deviations (%) of (a)  $\beta_{M532}$ , (b)  $\delta_p$ , and (c)  $\gamma$ .

There is a difference in the seasonal variations of  $\overline{\beta_{M532}}$  and  $\overline{\delta_p}$ , as shown in Figures 2 and 3. Figure 6b shows the averaged  $\delta_p$  at 532 nm for the same months throughout the four years of the observations,  $\overline{\delta_p}$ .  $\overline{\delta_p}$  showed larger values at altitudes between 2 and 8 km from January to May when  $\overline{\beta_{M532}}$  was increasing (Figures 6a and 6b), as described in section 4.

The  $\overline{\delta_p}$  and  $\overline{\delta_p}$  values reached a maximum value of several percent and were less than 3% at most altitudes until the end of 2017. The values of  $\overline{\delta_p}$  and  $\overline{\delta_p}$  were nearly zero below an altitude of 4 km,

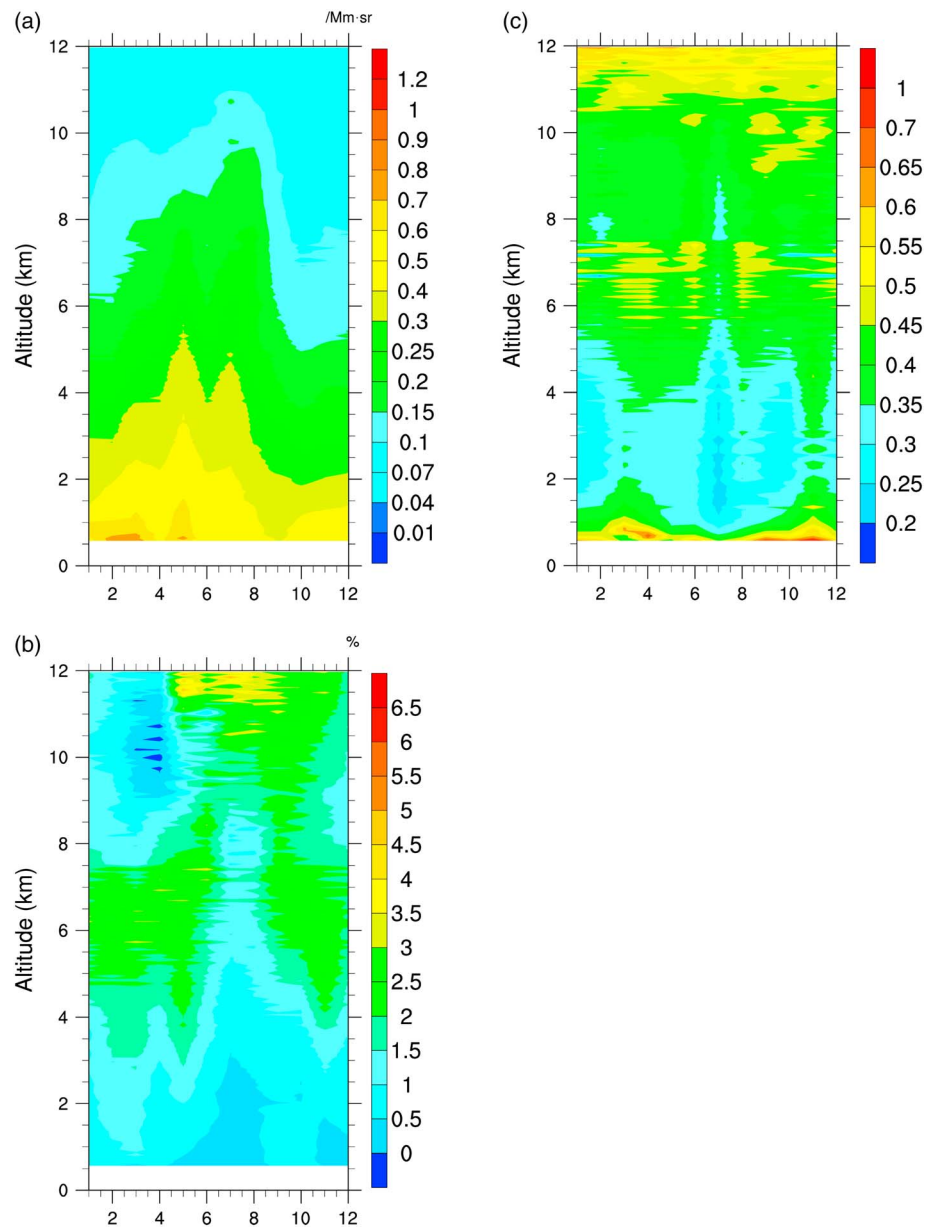


**Figure 6.** Averaged  $\beta_{M532}$ ,  $\delta_\rho$ , and  $\gamma$  for the same months throughout the four years of the observations: (a)  $\overline{\beta_{M532}}$ , (b)  $\overline{\delta_\rho}$ , and (c)  $\overline{\gamma}$  from March 2014 to December 2017.

especially during the summer months;  $\overline{\delta_\rho}$  had minimum values in July and August (Figure 6b), corresponding to the largest lidar-observed  $\overline{\beta_{M532}}$  values (Figure 6a). Observations in the Arctic boundary layer have shown active particle formation during the summer (Collins et al., 2017; Freud et al., 2017; Tunved et al., 2013). At higher altitudes, Scheuer et al. (2003) reported a sharp increase in the mixing ratio of sulfate ions in free tropospheric fine aerosol particles over the Arctic during March. Even though their measurements ended in May, the upper tropospheric mixing ratio of the sulfate ions was highest in May.

Figure 6c shows the averaged  $\gamma$  for the same months throughout the four years of the observations,  $\overline{\gamma}$ . The decrease in  $\overline{\gamma}$  corresponds to a decrease in the particle size (Shibata & Yang, 2010). The variation in  $\overline{\gamma}$  is likely in agreement with the results of the color ratio of the extinction observed by SAGE (Figure 8 in Treffeisen et al., 2006). The variations in  $\overline{\delta_\rho}$  (Figure 6b) and  $\overline{\gamma}$  (Figure 6c) show a weak positive correlation

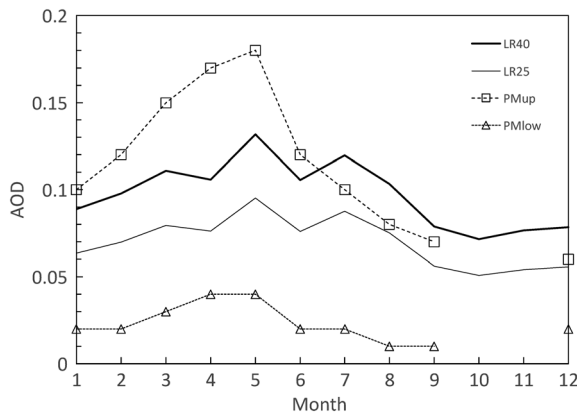


**Figure 7.** The aerosol optical depth (AOD), which vertically integrates the data in Figure 6a and multiplies by the lidar ratio for altitudes between 0.6 and 12 km. The bold (LR40) and thin (LR25) solid lines are the AODs with assumed lidar ratios of 40 and 25 sr, respectively. The broken and dotted lines with squares (PMup) and triangles (PMlow) show the roughly estimated upper and lower limits, respectively, of the photometer-observed AOD in Figure 7 in Herber et al. (2002).

in the altitude range between 2 and 10 km, and a correlation between these two parameters can generally be expected due to the scattering characteristics of the particles (Shibata & Yang, 2010).

A small percentage of  $\delta_p$  could be caused by many types of aerosols, such as anthropogenic, marine, biomass-burning-produced, or dust (Burton et al., 2013; Groß et al., 2011, 2013; Illingworth et al., 2015) and their external or internal mixtures.  $\overline{\delta_p}$  began increasing in January at altitudes from 2 to 4 km (Figure 3b). Because biomass burning and dust events are not common in January (e.g., Kurosaki & Mikami, 2003; Macias Fauria & Johnson, 2008), the particles from such sources likely contributed very little to the winter increase in  $\overline{\delta_p}$ .

Hara et al. (2003) used electron microscopy to study the mixing state of aerosol particles using samples taken over Svalbard via an airplane several times in March and April 2000. They found that highly acidic, liquid-phase sulfate (likely sulfuric acid) and soot particles were the major aerosol particles under background and Arctic haze conditions and that the soot particles were mostly externally mixed with the sulfate particles. Mineral dust particles were also observed; however, their frequency was much smaller. Sea-salt particles were found only in the lower troposphere below

an altitude of 3 km and in deliquesced form. Even though the observations by Hara et al. (2003) were only performed in the spring, their results are consistent with the lidar-observed low  $\delta_p$  and its increase in the spring. Because the particles composed of sulfate were observed in their liquid form, the  $\delta_p$  of these particles is zero if they are not internally mixed with solid particles. Mishchenko et al. (2017) estimated that the depolarization ratio caused by soot particles at a wavelength of 532 nm is approximately 10%. In Figure 5 in Hara et al. (2003), the relative abundance of soot particles ranged from a few percent to more than 90% and was a few tens of percent on average. At an abundance of a few tens of percent, the depolarization ratio of all externally mixed liquid sulfate and soot aerosol particles was a few percent (e.g., Shibata & Yang, 2010). Therefore, the soot particles could have contributed to the  $\delta_p$  increase during the spring.

The soot particles are likely anthropogenic and transported from Europe or Russia, as suggested by Hara et al. (2003). If the liquid-phase sulfate particles increase in the following summer season via particle formation without increasing the soot particles due to less active transport from lower latitudes,  $\delta_p$  decreases, as was observed by the lidar observations. Further studies sampling the free troposphere, especially during non-spring months, are needed to determine the cause of the lidar-observed seasonal variations. Willis et al. (2018) indicated that the abundance of organic constituents is comparable to sulfate in the lower free troposphere. Because aerosols including organic species are likely to be in the liquid phase (Marcolli et al., 2004), the above discussion is also valid when the aerosols include organic species.

The seasonal variations in the  $\delta_p$  values could also have been caused by the contamination of insufficiently rejected cloud components in the data. However, this is unlikely because CALIPSO observed a low seasonality of cloud occurrences at tropospheric heights over Svalbard (Hagihara & Okamoto, 2003). In addition, even in the case of subvisible cirrus clouds often observed over the Arctic, their backscattering coefficients are larger than our cloud selection threshold.

## 6. Summary and Conclusions

Four years of ground-based Mie depolarization lidar observations of aerosols in the free troposphere at the high Arctic observational site of Ny-Ålesund (79°N 12°E), Svalbard, were presented. The monthly averaged vertical distribution of backscattering coefficients indicated that the mass concentration of aerosols was largest in the lowest free troposphere and was an order of magnitude smaller in the highest free troposphere;  $\overline{\beta_{M532}}$  was 0.5–1/Mm·sr at altitudes lower than 1 km and 0.1–0.2/Mm·sr at an altitude of 10 km. The clear seasonal cycle of  $\overline{\beta_{M532}}$  in the free troposphere presented the highest concentrations of aerosols in late spring and summer and the lowest concentrations in late summer and fall. At altitudes higher than 4 km in the free troposphere,  $\overline{\beta_{M532}}$  reached a maximum from May to July. The monthly mean particle depolarization ratio  $\overline{\delta_p}$

remained below a few percent year-round. Furthermore,  $\overline{\delta_p}$  was largest during the winter and spring at altitudes from 5 to 8 km and smallest (nearly 0%) during the summer at altitudes lower than 4 km. The largest values of  $\overline{\delta_p}$  preceded the largest values of  $\overline{\beta_{M532}}$  by a few months, possibly indicating changes in the physical or chemical characteristics of the aerosol particles during these seasons or the springtime replacement of slightly depolarizing particles by nondepolarizing smaller-sized particles in the free troposphere in association with changes in the seasonal meteorological conditions. The low values of  $\overline{\delta_p}$  were consistent with the mixing of liquid phase sulfate and soot particles reported by previous studies. The variation in  $\overline{\gamma}$  appeared to be correlated with the variation in  $\overline{\delta_p}$ , as expected from scattering theory.

## Glossary

$\beta_{M\lambda}$	backscattering coefficient of aerosols at wavelength $\lambda$
$R_\lambda$	backscatter ratio at wavelength $\lambda$
$R_0$	$R_{532}$ averaged at altitudes between 12 and 15 km
$\gamma$	color ratio
$\delta_V$	volume depolarization ratio
$g$	factor to adjust the sensitivity of the two polarization signal components
$\delta'_V$	volume depolarization ratio estimated from the observed signal
$\delta_{am}$	depolarization ratio of the atmospheric molecules
$\delta_p$	particle depolarization ratio
RSD	relative standard deviation

## Appendix A: Cloud Removal Procedure

Successive 1-min profiles without cloud signals were selected using the following method taking into account the study by Liu et al. (2004). (1) Because the backscattering coefficient of clouds is usually orders of magnitude larger than that of aerosols, from the time-height plots (e.g., Figure 1a), 1-min profiles were selected without altitude ranges whose Rayleigh-backscattering-coefficient-subtracted attenuated-backscattering coefficient without correction for attenuation at a wavelength of 1,064 nm,  $\beta'_{M1064}$ , was larger than  $1.0 \times 10^{-5}$ /m-sr. (2) Within the profiles selected using condition (1), we further selected the profiles that did not have an altitude range where  $\beta'_{M1064}$  was larger than  $1.0 \times 10^{-6}$ /m-sr and could reach that selected by condition (1),  $\beta'_{M1064} > 1.0 \times 10^{-5}$ /m-sr, following the successive ranges of the 1-min profiles whose  $\beta'_{M1064}$  was larger than  $1.0 \times 10^{-6}$ /m-sr.

In addition, the altitude of the daily averaged profiles was not included in the monthly mean when  $\delta_p$  was larger than 0.3, the typical value for cirrus clouds (Shibata et al., 2012). However, this condition had very little impact on the results.

## Appendix B: Factor $g$

The factor  $g$  was obtained experimentally using the method of Freudenthaler et al. (2009) as follows. For the experiments only, we placed an additional polarization filter in front of the polarization prism that separates the perpendicular and parallel components. By setting the polarization angle of the filter to  $45^\circ$  with respect to the polarization plane of the laser pulses, we can expect the same intensity of the signal at the detectors for each polarization component. Therefore, the difference in the measured intensity of the signal with this setting is caused by the difference in the detection sensitivity. This factor is determined via  $g = P_{\parallel}(\text{with } 45^\circ \text{ filter})/P_{\perp}(\text{with } 45^\circ \text{ filter})$  using the measured signal with the additional polarization filter. The evaluated value of  $g$  for our system is a few percent larger than 1.0.

## Appendix C: Estimation of $\delta_V$ From the Observed $\delta'_V$

Adachi et al. (2001) indicated a method to retrieve  $\delta_V$  from the  $\delta'_V$  obtained by an actual lidar system and showed that the relationship between  $\delta_V$  and  $\delta'_V$  is

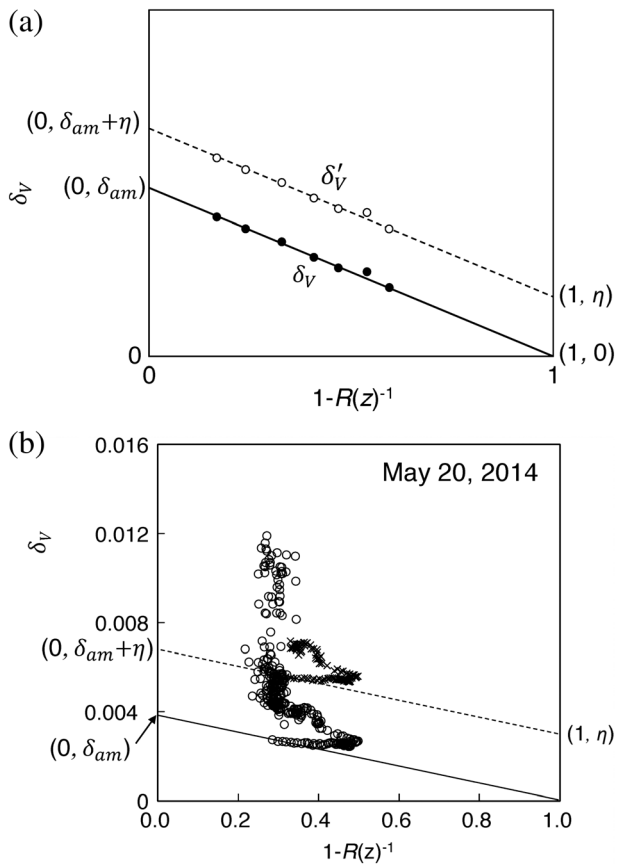


**Figure A1.** (a) A schematic showing the relationship between  $\delta'_V$  (open circles) and the offset-corrected  $\delta_V$  (black circles) of spherical particles. (b) An example of observed  $\delta'_V$  (cross) and offset-corrected  $\delta_V$  (open circles) on 20 May 2014. In (b),  $\delta'_V$  (cross) points are plotted for the altitude range between 0.6 and 2.0 km and  $\delta_V$  (open circles) points are plotted between 0.6 and 5.0 km.

$$\delta_V = (1 + 2\eta)\delta'_V - \eta, \quad (\text{A1})$$

where  $\eta$  is a constant number. Because  $\eta$  and  $\delta'_V$  are on the order of 0.01, we can further approximate equation (A1) as

$$\delta_V = \delta'_V - \eta. \quad (\text{A2})$$

In other words,  $\delta'_V$  of an actual lidar system is offset from the defined  $\delta_V$  by  $\eta$ . Adachi et al. proposed a two-dimensional scattering plot of  $(1 - R(z)^{-1}, \delta'_V(z))$  to estimate the value of  $\eta$ . They indicated that the scattering plots  $(1 - R(z)^{-1}, \delta'_V(z))$  of aerosols with 0% depolarization of the spherical (liquid) particles plot on a line expressed by

$$\delta'_V(x) = (1 - x)\delta_{am} + \eta, \quad (\text{A3})$$

where  $x = 1 - R(z)^{-1}$ . If 0% depolarization aerosols are observed by the actual nonideal lidar system described above, the scattering plot of  $(1 - R(z)^{-1}, \delta'_V(z))$  is on the line connecting  $(0, \delta_{am} + \eta)$  and  $(1, \eta)$ .

Adachi et al. used observational data to estimate  $\eta$ . Under atmospheric conditions in which spherical (or liquid with 0% depolarization ratio) aerosols exist, if we find a group of points that is nearly on a line whose slope is  $-\delta_{am}$ , the value of this line at  $x = 1$  gives  $\eta$  and  $\delta_V$  is obtained via equation (A2), that is, by subtracting  $\eta$  from  $\delta'_V$ . Figure A1a schematically shows this relationship between  $\delta_V$  and  $\delta'_V$  for spherical particles. After performing this offset correction,  $\delta_p(z)$  was obtained from  $\delta_V(z)$  and  $R(z)$  as in equation (7) in the text. The atmospheric depolarization ratio  $\delta_{am}$  is estimated using scattering theory and is 0.0038 for the bandwidth of the interference filter, 0.3-nm FWHM, used in our lidar system (e.g., Adachi et al., 2001; Cairo et al., 1999).

In most cases, we were able to determine the altitude range where the slope of the plotted points of  $(1 - R(z)^{-1}, \delta'_V(z))$  was  $-\delta_{am}$ . This altitude

range is generally lower than 2 km, and we expect deliquesced sea salt particles to be the spherical liquid particles resulting in  $\delta_p = 0$  in the environment of Svalbard, which is surrounded by the Arctic Sea (Hara et al., 2003). Figure A1b shows observed plots of  $\delta'_V$  and the offset-corrected  $\delta_V$  for the case on 20 May 2014. In Figure A1b,  $\delta_V$  (open circle) points are plotted between 0.6 and 5.0 km, whereas  $\delta'_V$  (cross) points are plotted in a smaller altitude range between 0.6 and 2.0 km for ease of viewing. The  $\eta$  values obtained using this method are mostly between  $-0.005$  and  $0.005$ . After this correction,  $\delta_p$  changes a few times with the opposite sign of  $\eta$ .

#### Acknowledgments

We thank the Arctic Environment Research Center (AERC) of the National Institute of Polar Research (NIPR) for providing us the facilities to conduct our research at Ny-Ålesund. We also thank the staff of Kings Bay AS for their help to continue the observations. We thank the anonymous three reviewers for their comments in improving the manuscript. This study was supported by the Japan Society for the Promotion of Science (JSPS) KAKENHI grants (25257201 and 16H02702). The data used in this study will be available from the Arctic Data archive System (ADS, <https://ads.nipr.ac.jp>), NIPR.

#### References

- Adachi, H., Shibata, T., Iwasaka, Y., & Fujiwara, M. (2001). Calibration method for the lidar-observed stratospheric depolarization ratio in the presence of liquid aerosol particles. *Applied Optics*, *40*(36), 6587–6595. <https://doi.org/10.1364/AO.40.006587>
- Breider, T. J., Mickley, L. J., Jacob, D. J., Ge, C., Wang, J., Sulprizio, M. P., et al. (2017). Multidecadal trends in aerosol radiative forcing over the Arctic: Contribution of changes in anthropogenic aerosol to Arctic warming since 1980. *Journal of Geophysical Research: Atmospheres*, *122*, 3573–3594. <https://doi.org/10.1002/2016JD025321>
- Breider, T. J., Mickley, L. J., Jacob, D. J., Wang, Q. Q., Fisher, J. A., Chang, R. Y. W., & Alexander, B. (2014). Annual distributions and sources of Arctic aerosol components, aerosol optical depth, and aerosol absorption. *Journal of Geophysical Research: Atmospheres*, *119*, 4107–4124. <https://doi.org/10.1002/2013JD020996>
- Burton, S. P., Ferrare, R. A., Vaughan, M. A., Omar, A. H., Rogers, R. R., Hostetler, C. A., & Hair, J. W. (2013). Aerosol classification from airborne HSRL and comparisons with the CALIPSO vertical feature mask. *Atmospheric Measurement Techniques*, *6*(5), 1397–1412. <https://doi.org/10.5194/amt-6-1397-2013>
- Cairo, F., Di Donfrancesco, G., Adriani, A., Pulvirenti, L., & Fierli, F. (1999). Comparison of various linear depolarization parameters measured by lidar. *Applied Optics*, *38*(21), 4425–4432. <https://doi.org/10.1364/AO.38.004425>

- Cattrell, C., Reagan, J., Thome, K., & Dubovik, O. (2005). Variability of aerosol and spectral lidar and backscatter and extinction ratios of key aerosol types derived from selected Aerosol Robotic Network locations. *Journal of Geophysical Research*, *110*, D10S11. <https://doi.org/10.1029/2004JD005124>
- Collins, D. B., Burkar, J., Chang, R. Y.-W., Lizotte, M., Boivin-Rioux, A., Blais, M., et al. (2017). Frequent ultrafine particle formation and growth in Canadian Arctic marine and coastal environments. *Atmospheric Chemistry and Physics*, *17*(21), 13,119–13,138. <https://doi.org/10.5194/acp-17-13119-2017>
- Di Piero, M., Jaeglé, L., Eloranta, E. W., & Sharma, S. (2013). Spatial and seasonal distribution of Arctic aerosols observed by the CALIOP satellite instrument (2006–2012). *Atmospheric Chemistry and Physics*, *13*(14), 7075–7095. <https://doi.org/10.5194/acp-13-7075-2013>
- Dubovik, O., Smirnov, A., Holben, B. N., King, M. D., Kaufman, Y. J., Eck, T. F., & Slutsker, I. (2000). Accuracy assessments of aerosol optical properties retrieved from AERONET sun and sky-radiance measurements. *Journal of Geophysical Research*, *105*, 9791–9806. <https://doi.org/10.1029/2000JD900040>
- Fernald, F. G. (1984). Analysis of atmospheric lidar observations: Some comments. *Applied Optics*, *23*(5), 652–653. <https://doi.org/10.1364/AO.23.000652>
- Freud, E., Krejci, R., Tunved, P., Leaitch, R., Nguyen, Q. T., Massling, A., et al. (2017). Pan-Arctic aerosol number size distributions: Seasonality and transport patterns. *Atmospheric Chemistry and Physics*, *17*(13), 8101–8128. <https://doi.org/10.5194/acp-17-8101-2017>
- Freudenthaler, V., Esselborn, M., Wiegner, M., Heese, B., Tesche, M., Ansmann, A., et al. (2009). Depolarization ratio profiling at several wavelengths in pure Saharan dust during SAMUM 2006. *Tellus B*, *61*(1), 165–179. <https://doi.org/10.1111/j.1600-0889.2008.00396.x>
- Groß, S., Esselborn, M., Weinzierl, B., Wirth, M., Fix, A., & Petzold, A. (2013). Aerosol classification by airborne high spectral resolution lidar observations. *Atmospheric Chemistry and Physics*, *13*(5), 2487–2505. <https://doi.org/10.5194/acp-13-2487-2013>
- Groß, S., Tesche, M., Freudenthaler, V., Toledano, C., Wiegner, M., Ansmann, A., et al. (2011). Characterization of Saharan dust, marine aerosols and mixtures of biomass-burning aerosols and dust by means of multi-wavelength depolarization and Raman lidar measurements during SAMUM 2. *Tellus B*, *63*(4), 706–724. <https://doi.org/10.1111/j.1600-0889.2011.00556.x>
- Hagihara, Y., & Okamoto, H. (2003). Global cloud distribution revealed by combined use of CloudSat/CALIPSO: Comparison using CALIPSO versions 2 and 3 data. *AIP Conference Proceedings*, *1531*, 456–459. <https://doi.org/10.1063/1.4804805>
- Hara, K., Yamagata, S., Yamanouchi, T., Sato, K., Herber, A., & Iwasaka, et al. (2003). Mixing states of individual aerosol particles in spring Arctic troposphere during ASTAR 2000 campaign. *Journal of Geophysical Research*, *108*(D7), 4209. <https://doi.org/10.1029/2002JD002513>
- Herber, A., Thomason, L. W., Gernandt, H., Leiterer, U., Nagel, D., Schulz, K.-H., et al. (2002). Continuous day and night aerosol optical depth observations in the Arctic between 1991 and 1999. *Journal of Geophysical Research*, *107*(D10), 4097. <https://doi.org/10.1029/2001JD000536>
- Illingworth, A. J., Barker, H. W., Beljaars, A., Ceccaldi, M., Chepfer, H., Clerbaux, N., et al. (2015). The EarthCARE satellite: The next step forward in global measurements of clouds, aerosols, precipitation, and radiation. *Bulletin of the American Meteorological Society*, *96*(8), 1311–1332. <https://doi.org/10.1175/BAMS-D-12-00227.1>
- Ishii, S., Shibata, T., Nagai, T., Mizutani, K., Itabe, T., Hirota, M., et al. (1999). Arctic haze and clouds observed by lidar during four winter seasons of 1993–1997, at Eureka, Canada. *Atmospheric Environment*, *33*(16), 2459–2470. [https://doi.org/10.1016/S1352-2310\(98\)00397-5](https://doi.org/10.1016/S1352-2310(98)00397-5)
- Ishii, S., Shibata, T., Sakai, T., Kido, M., Hara, K., Osada, K., et al. (2001). The source, size and chemical composition of the winter Arctic tropospheric aerosol layer observed by lidar at Eureka, Canada. *Journal of the Meteorological Society of Japan*, *79*(1), 61–78. <https://doi.org/10.2151/jmsj.79.61>
- Kurosaki, Y., & Mikami, M. (2003). Recent frequent dust events and their relation to surface wind in East Asia. *Geophysical Research Letters*, *30*(14), 1736. <https://doi.org/10.1029/2003GL017261>
- Leaitch, W. R., Hoff, R. M., & MacPherson, J. I. (1986). Airborne and lidar measurements of aerosol and cloud particles in the troposphere over Alert Canada in April 1986. *Journal of Atmospheric Chemistry*, *9*(1-3), 187–211. <https://doi.org/10.1007/BF00052832>
- Lisok, J., Rozwadowska, A., Pedersen, J. G., Markowicz, K. M., Ritter, C., Kaminski, J. W., et al. (2018). Radiative impact of an extreme Arctic biomass-burning event. *Atmospheric Chemistry and Physics*, *18*(12), 8829–8848. <https://doi.org/10.5194/acp-18-8829-2018>
- Liu, Z., Vaughan, M. A., Winker, D. M., Hostetler, C. A., Poole, L. R., Hlavka, D., et al. (2004). Use of probability distribution functions for discriminating between cloud and aerosol in lidar backscatter data. *Journal of Geophysical Research*, *109*, D15202. <https://doi.org/10.1029/2004JD004732>
- Macias Fauria, M., & Johnson, E. A. (2008). Climate and wildfires in the North American boreal forest. *Philosophical Transactions of the Royal Society B*, *363*(1501), 2315–2327. <https://doi.org/10.1098/rstb.2007.2202>
- Marcolli, C., Luo, B., & Peter, T. (2004). Mixing of the organic aerosol fractions: Liquids as the thermodynamically stable phases. *The Journal of Physical Chemistry. A*, *108*(12), 2216–2224. <https://doi.org/10.1021/jp036080l>
- Mishchenko, M. I., Dlugach, J. M., & Liu, L. (2017). Linear depolarization of lidar returns by aged smoke particles. *Applied Optics*, *55*(35), 9968–9973. <https://doi.org/10.1364/AO.55.009968>
- Najafi, M. R., Zwiers, F. W., & Gillett, N. P. (2015). Attribution of Arctic temperature change to greenhouse-gas and aerosol influences. *Nature Climate Change*, *5*(3), 246–249. <https://doi.org/10.1038/nclimate2524>
- Nott, J. G., & Duck, T. J. (2011). Lidar studies of the polar troposphere. *Meteorological Applications*, *18*(3), 383–405. <https://doi.org/10.1002/met.289>
- Omar, A. H., Won, J.-G., Winker, D. M., Yoon, S.-C., Dubovik, O., & McCormick, M. P. (2005). Development of global aerosol models using cluster analysis of Aerosol Robotic Network (AERONET) measurements. *Journal of Geophysical Research*, *110*, D10S14. <https://doi.org/10.1029/2004JD004874>
- Pappalardo, G., Amodeo, A., Apituley, A., Comeron, A., Freudenthaler, V., Linné, H., et al. (2014). EARLINET: Towards an advanced sustainable European aerosol lidar network. *Atmospheric Measurement Techniques*, *7*(8), 2389–2409. <https://doi.org/10.5194/amt-7-2389-2014>
- Platt, C. M. R., Abshire, N. L., & McNice, G. T. (1978). Some microphysical properties of an ice cloud from lidar observation of horizontally oriented crystals. *Journal of Applied Meteorology*, *17*(8), 1220–1224. [https://doi.org/10.1175/1520-0450\(1978\)017<1220:SMPOAI>2.0.CO;2](https://doi.org/10.1175/1520-0450(1978)017<1220:SMPOAI>2.0.CO;2)
- Quinn, P. K., Shaw, G., Andrews, E., Dutton, E. G., Ruoho-Airola, T., & Gong, S. L. (2007). Arctic haze: Current trends and knowledge gaps. *Tellus*, *59*(1), 115–129. <https://doi.org/10.1111/j.1600-0889.2006.00236.x>
- Ritter, C., Neuber, R., Schulz, A., Markowicz, K. M., Stachlewska, I. S., Lisok, J., et al. (2016). 2014 iAREA campaign on aerosol in Spitsbergen e part 2: Optical properties from Raman-lidar and in-situ observations at Ny-Ålesund. *Atmospheric Environment*, *141*, 1–19. <https://doi.org/10.1016/j.atmosenv.2016.05.053>
- Russell, P. B., Swisler, T. J., & McCormick, M. P. (1979). Methodology for error analysis and simulation of lidar aerosol measurements. *Applied Optics*, *18*(22), 3783–3797. <https://doi.org/10.1364/AO.18.003783>

- Sakai, T., Uchino, O., Nagai, T., Liley, B., Morino, I., & Fujimoto, T. (2016). Long-term variation of stratospheric aerosols observed with lidars over Tsukuba, Japan, from 1982 and Lauder, New Zealand, from 1992 to 2015. *Journal of Geophysical Research: Atmospheres*, *121*, 10,283–10,293. <https://doi.org/10.1002/2016JD025132>
- Scheuer, E., Talbot, R. W., Dibb, J. E., Seid, G. K., DeBell, L., & Lefer, B. (2003). Seasonal distributions of fine aerosol sulfate in the North American Arctic basin during TOPSE. *Journal of Geophysical Research*, *108*(D4), 8370. <https://doi.org/10.1029/2001JD001364>
- Shaw, G. E. (1975). The vertical distribution of tropospheric aerosols at Barrow, Alaska. *Tellus*, *27*(1), 39–50. <https://doi.org/10.3402/tellusa.v27i1.9882>
- Shaw, G. E. (1995). The Arctic haze phenomenon. *Bulletin of the American Meteorological Society*, *76*(12), 2403–2413. [https://doi.org/10.1175/1520-0477\(1995\)076<2403:TAHP>2.0.CO;2](https://doi.org/10.1175/1520-0477(1995)076<2403:TAHP>2.0.CO;2)
- Shibata, T., Hayashi, M., Naganuma, A., Hara, N., Hara, K., Hasebe, F., et al. (2012). Cirrus cloud appearance in a volcanic aerosol layer around the tropical cold point tropopause over Biak, Indonesia, in January 2011. *Journal of Geophysical Research*, *117*, D11209. <https://doi.org/10.1029/2011JD017029>
- Shibata, T., Shiraishi, K., Adachi, H., Iwasaka, Y., & Fujiwara, M. (1999). On the lidar observed sandwich structure of polar stratospheric clouds, I, implications for the mixing state of the PSC particles. *Journal of Geophysical Research*, *104*, 21,603–21,611. <https://doi.org/10.1029/1999JD900333>
- Shibata, T., & Yang, Y. (2010). Decrease in depolarization of dust over populated areas of eastern Asia observed by the space-borne Lidar CALIOP. *Eurozoru Kenkyu*, *25*(1), 62–76. <https://doi.org/10.11203/Jar.25.62>
- Shimizu, A., Sugimoto, N., Matsui, I., Nishizawa, T., & Jin, Y. (2016). Activities in 15 years of AD-Net, a lidar network for Asian dust studies. *ProScience*, *3*, 106–110. <https://doi.org/10.14644/dust.2016.017>
- Treffeisen, R. E., Thomason, L. W., Ström, J., Herber, A. B., Burton, S. P., & Yamanouchi, T. (2006). Stratospheric Aerosol and Gas Experiment (SAGE) II and III aerosol extinction measurements in the Arctic middle and upper troposphere. *Journal of Geophysical Research*, *111*, D17203. <https://doi.org/10.1029/2005JD006271>
- Tunved, P., Ström, J., & Krejci, R. (2013). Arctic aerosol life cycle: Linking aerosol size distributions observed between 2000 and 2010 with air mass transport and precipitation at Zeppelin station, Ny-Ålesund, Svalbard. *Atmospheric Chemistry and Physics*, *13*(7), 3643–3660. <https://doi.org/10.5194/acp-13-3643-2013>
- Willis, M. D., Bozem, H., Kunkel, D., Lee, A. K. Y., Schulz, H., Burkart, J., et al. (2018). Aircraft measurements of high Arctic springtime aerosol show evidence for vertically varying sources, transport and composition. *Atmospheric Chemistry and Physics Discussions*, 1–32. <https://doi.org/10.5194/acp-2018-628>
- Winker, D. M., Vaughan, M. A., Omar, A., Hu, Y., Powell, K. A., Liu, Z., et al. (2009). Overview of the CALIPSO mission and CALIOP data processing algorithms. *Journal of Atmospheric and Oceanic Technology*, *26*(11), 2310–2323. <https://doi.org/10.1175/2009JTECHA1281.1>